JGR Oceans

AGU ADVANCING EARTH AND SPACE SCIENCE

Sub-Ice Platelet Layer Physics: Insights From a Mushy-Layer Sea Ice Model

P. Wongpan[1,2,3,4] , M. Vancoppenolle[5] , P. J. Langhorne[1] , I. J. Smith[1] , G. Madec[5,6] , A. J. Gough[1], A. R. Mahoney[7] , and T. G. Haskell[8]

[1]Department of Physics, University of Otago, Dunedin, New Zealand, [2]Institute of Low Temperature Science, Hokkaido University, Sapporo, Japan, [3]JSPS International Research Fellow, Japan Society for the Promotion of Science, Tokyo, Japan, [4]Now at Australian Antarctic Program Partnership, Institute for Marine and Antarctic Studies, University of Tasmania, Hobart, Tasmania, Australia, [5]Sorbonne Université, LOCEAN-IPSL, CNRS/IRD/MNHN, Paris, France, [6]University Grenoble Alpes, CNRS, INRIA, CNRS, Grenoble INP, LJK, Grenoble, France, [7]Geophysical Institute, University of Alaska Fairbanks, Fairbanks, AK, USA, [8]Callaghan Innovation, Lower Hutt, New Zealand

Abstract The sub-ice platelet layer (SIPL) is a highly porous, isothermal, friable layer of ice crystals and saltwater, that can develop to several meters in thickness under consolidated sea ice near Antarctic ice shelves. While the SIPL has been comprehensively described, details of its physics are rather poorly understood. In this contribution we describe the halo-thermodynamic mechanisms driving the development and stability of the SIPL in mushy-layer sea ice model simulations, forced by thermal atmospheric and oceanic conditions in McMurdo Sound, Ross Sea, Antarctica. The novelty of these simulations is that they predict a realistic model analogue for the SIPL. Two aspects of the model are essential: (a) a large initial brine fraction is imposed on newly forming ice, and (b) brine rejection via advective desalination. The SIPL appears once conductive heat fluxes become insufficient to remove latent heat required to freeze the highly porous new ice. Favorable conditions for SIPL formation include cold air, supercooled waters, and consolidated ice and snow that are thick enough to provide sufficient thermal insulation. Thermohaline properties resulting from large liquid fractions stabilize the SIPL, in particular a low thermal diffusivity. Intense convection within the isothermal SIPL generates the SIPL-consolidated ice contrast without transporting heat. Using standard physical constants and free parameters, the model successfully predicts the SIPL and consolidated ice thicknesses at six locations. While most simulations were performed with 50 layers, an SIPL emerged with moderate accuracy in thickness for three layers proving a low-cost representation of the SIPL in large-scale climate models.

Plain Language Summary The sub-ice platelet layer (SIPL) is a typical feature beneath sea ice near the Antarctic coast. The SIPL, made of ∼10 cm-large ice crystals bathed in salt water, can be several meters thick and harbor exceptionally prolific micro-algae. Much of coastal Antarctica is occupied by massive glaciers that float upon the ocean. We know that meltwater, released by glacial melting at depth, rises and refreezes on its ascent, sourcing ice to the SIPL. Yet many aspects of the growth and decay of an SIPL are poorly understood. Here, we present the first realistic simulations of the SIPL phenomenon near McMurdo Sound, Antarctica, based on a computer model encapsulating state-of-the-art sea ice physics. The simulations inform us of features within the SIPL that are difficult to observe directly and help us understand why the SIPL is common, thick, and long-lasting. In our simulations, the large volume of saltwater bathing the SIPL crystals buffers heat transfer and favors salt transfer, stabilizing the SIPL and generating a contrast with the consolidated sea ice above the SIPL. We also suggest a method of achieving an SIPL in climate models, which will help define its role in polar climate and ecology.

1. Introduction

Antarctic fast ice mainly forms as a result of heat loss to the atmosphere. However, close to an ice shelf, fast ice also grows due to heat loss to the water column, resulting in a sub-ice platelet layer (SIPL) that can commonly reach several meters in thickness (Hoppmann et al., 2020; Hughes et al., 2014; Hoppmann, Nicolaus, Hunkeler, et al., 2015; Langhorne et al., 2015). An SIPL is one of the most extraordinary, yet poorly understood, features of the coastal Antarctic marine environment, harboring a very productive community of micro-organisms (Arrigo, 2017; Günther & Dieckmann, 1999).
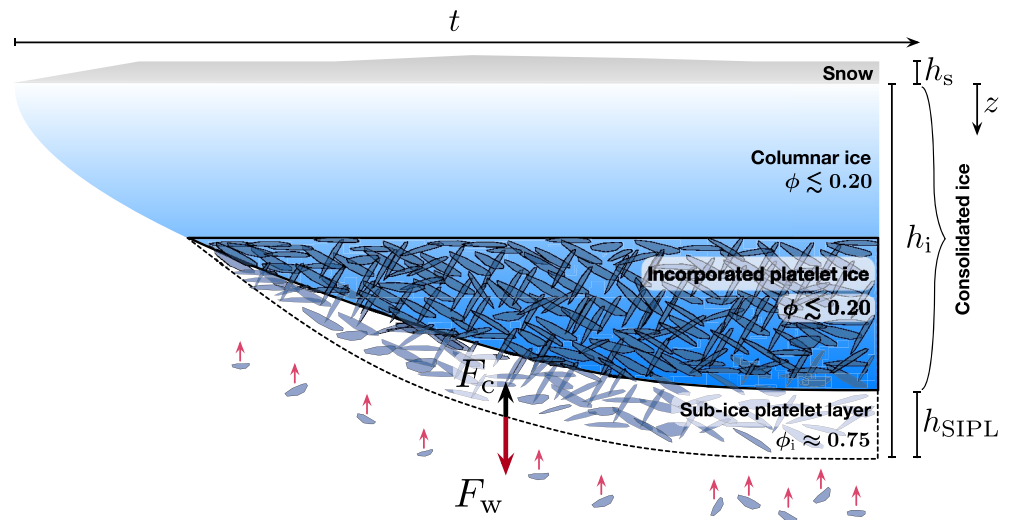
Figure 1. Schematic of a typical sea ice growth season (with time, *t*, running left to right) near a cold-cavity ice shelf, with snow on top, columnar ice, incorporated platelet ice, and the highly porous sub-ice platelet layer. F_c and F_w are the conductive and sensible oceanic heat fluxes, respectively; h_s is snow depth, h_i is total ice thickness, h_{SIPL} is the sub-ice platelet layer thickness. Consolidated ice, with relatively low brine fraction, is composed of columnar ice and of incorporated platelet ice.

Platelet ice growth happens where supercooled Ice Shelf Water (ISW) contacts the sea ice-ocean interface (e.g., Gow et al., 1998; Leonard et al., 2006; McPhee et al., 2016). ISW is found where an ice shelf feeds the deep ocean with buoyant meltwater. The meltwater becomes supercooled on its journey along the ice shelf base toward the sea ice on the ocean's surface. New ice crystals can form locally, close to the sea ice-ocean interface. Alternatively, the buoyant frazil crystals might first appear deeper in the water column and subsequently move upwards to accumulate under the sea ice. There they grow in-situ due to heat loss to the ocean and/or to the atmosphere (Gough, Mahoney, Langhorne, Williams, Robinson, et al., 2012; Hughes et al., 2014; Smith et al., 2012). These remote and in-situ sources of heat loss are difficult to separate and are often counted together as a negative oceanic heat flux applied directly at the base of sea ice (Gough, Mahoney, Langhorne, Williams, Robinson, et al., 2012; Langhorne et al., 2015). Initially, platelet ice crystals intertwine in a highly porous, friable, unconsolidated, layer of ice crystals and saltwater, referred to as the SIPL. Subsequent freezing of water in the interstices between crystals generates the consolidated, incorporated platelet ice, as illustrated in Figure 1.

The large-scale coverage and seasonal cycle of platelet ice, and its role in Southern Ocean dynamics and ecology are poorly constrained through observations (Hoppmann et al., 2020). Physically based model representations have the potential to improve this understanding. Yet, at present platelet ice modeling is in its infancy (Buffo et al., 2018; Cheng et al., 2019; Dempsey et al., 2010; Wongpan et al., 2015). As a result, platelet ice is neither a parameterized nor an emergent property of the sea ice cover in Earth System Model simulations (Steiner et al., 2016).

Modeling studies of platelet ice physics to date have treated several aspects of the problem of platelet ice formation. For instance, Wongpan et al. (2015) simulated the growth of an SIPL in three dimensions using heat and mass transfer at small scales (100 mm × 100 mm × 100 mm). They simulated a typical liquid fraction of ∼78% in the SIPL as an emergent property, which falls in the range of observational uncertainty (Gough, Mahoney, Langhorne, Williams, Robinson, et al., 2012; Hunkeler et al., 2016). Cheng et al. (2019) modified the two-dimensional, depth-integrated ISW plume model of Holland and Feltham (2006) for extension beneath sea ice, and compared the calculated thickness distribution of the SIPL with the measurements of Hughes et al. (2014). However, the required computational resources of these models limit their applicability at large spatial and temporal scales.

Among the simpler and less computationally expensive approaches for possible use in Earth System Models, that of Buffo et al. (2018) combines a representation of ice crystal nucleation and rise within the water

column with a 1D mushy-layer sea ice model. The model was tested in an idealized framework with supercooling as a tuned forcing. Their simulated thickness of the consolidated incorporated platelet ice layer agrees with observations at the end of the growth season (Dempsey et al., 2010), and, as expected, is tightly linked with the imposed supercooling. In one instance, their model also shows the development of an SIPL (their Figure 6). However, at this site in the conditions simulated, the SIPL was measured by Robinson et al. (2014) to be about 3 m-thick, in comparison with the Buffo et al. (2018) simulation of a few centimeters at most. While the modeling of Buffo et al. (2018) succeeds in regard to consolidated ice, it fails to capture the unconsolidated SIPL.

Many uncertainties and unknowns remain regarding the driving mechanisms of the SIPL and their possible representation in large-scale sea ice components for Earth System Models. In this contribution, we work toward answering the following questions. (a) Can a thermodynamic sea ice model (representative of an Earth System Model component) be adapted, adjusted, and realistically reproduce SIPL characteristics? (b) What does the model contribute to our understanding of the driving mechanisms in the SIPL? (c) Is the model sufficiently reliable to be used for large-scale investigations? In Section 2, we explain how we adjusted a mushy-layer sea ice model in order to tackle these questions. In Section 3, we describe the evaluation of the model, the simulated SIPL and the associated mechanisms. Results are discussed in Section 4 and conclusions are given in Section 5.

2. Data and Methods

In Section 2.1, we present the sea ice model used. In Section 2.2, we describe our simulation protocol, and the observational data from the fast ice near the McMurdo Ice Shelf. Notation used in the article is compiled in Table S1.

2.1. The Sea Ice Model

The model we use is Louvain-la-Neuve Sea Ice Model (LIM1D, http://forge.ipsl.jussieu.fr/lim1d, revision #3.20). The version we use is updated from Vancoppenolle et al. (2010) and Moreau et al. (2015). It is essentially based on mushy-layer physics (Notz & Worster, 2009; Worster, 1992), combining the Bitz and Lipscomb (1999; hereafter BL99) approach to thermodynamics with the Griewank and Notz (2013, 2015; hereafter GN1315) approach to salt dynamics. Constant ice density ρ_i is assumed. The model is based on finite differences, using N layers of equal thickness. The fundamental element of the model is a control mass of sea ice. The control mass is characterized by the two model state variables, temperature and salinity, that are functions of depth in the ice and time and evolve following the heat diffusion and salt transport equations. The sea ice phase composition, namely liquid fraction, follows from T and S, and in turn, controls the sea ice thermal properties.

Hereafter, we present generic elements relevant to the representation of platelet ice in one-dimensional, halo-thermodynamic sea ice models, for both unconsolidated (the SIPL) and consolidated (incorporated) platelet ice forms. The required model ingredients to capture an SIPL, are: (a) a liquid fraction-based formulation of sea-ice thermodynamics, (b) a sufficiently high initial liquid fraction, (c) convective gravity drainage (GN1315) and (d) a sufficiently negative oceanic heat flux. Each of these components is described in the following paragraphs.

2.1.1. Representing Unconsolidated Platelet Ice as High Liquid Fraction Sea Ice

Phase composition, in particular liquid (brine) fraction, is a very useful model feature to distinguish unconsolidated and consolidated platelet ice forms. Following BL99, LIM1D assumes sea ice to be made of pure ice and saline brine. This is justified because the sea ice crystalline lattice scarcely tolerates impurities at typically observed temperatures. Solid minerals and gas bubbles are ignored because they have a negligible contribution to sea ice mass and enthalpy. Under these hypotheses, the composition of sea ice is uniquely described by the brine (mass) fraction ϕ, while the pure ice fraction is $1 - \phi$. Here sea ice is to be understood as encompassing all possible forms of frozen seawater. We argue that this also includes the unconsolidated platelet ice of the SIPL, which we would expect to be characterized by liquid fractions in the 50%–100%

range, typically 75% (Langhorne et al., 2015); whereas consolidated platelet ice (incorporated platelet ice) and classical columnar ice forms would have more usual liquid fractions in the 0%–30% range.

Most sea ice properties are expressed as the sum of brine and pure ice contributions, weighted by brine and pure ice fractions. This applies to sea ice bulk salinity S, the salinity of a sufficiently large sea ice control mass. Since only brine inclusions contribute to bulk salinity,

$$S = \phi S_{br}, \tag{1}$$

where S_{br} is the brine salinity. We expect unconsolidated platelet ice would be characterized by large bulk salinity values, which would reflect the correspondingly large liquid fraction.

Thermal equilibrium between the liquid and solid phases is assumed, which is true in practice at sufficiently large time scales (>20 min). Hence, both phases have a single temperature T. In addition, brine inclusions must be at their freezing point. If not, ice would dissolve or freeze to restore equilibrium. Hence, if a linear salinity dependence of the freezing temperature is assumed, temperature and brine salinity relate through:

$$T = -\Gamma S_{br}, \tag{2}$$

where the liquidus slope $\Gamma = 0.054\,°C\left(g\,kg^{-1}\right)^{-1}$ (Assur, 1960). Combining Equations 1 and 2 gives

$$\phi = -\Gamma \frac{S}{T}, \tag{3}$$

which relates phase composition ϕ to bulk salinity and temperature, the two main sea ice state variables in this thermodynamic formulation. Equations 2 and 3 provide excellent approximations near the freezing point (Vancoppenolle et al., 2019) and therefore seem appropriate to represent unconsolidated platelet ice.

The vertical temperature field $T(z)$ derives from the resolution of the vertical heat equation. In the latter equation, the sea ice thermal properties include weighted contributions of brine and solid ice. Following Notz and Worster (2009), thermal conductivity is given by

$$k = k_{br}\phi + \left(1 - \phi\right)k_i, \tag{4}$$

where k_{br} is taken as 0.55 W m^{-1} K^{-1}, the thermal conductivity of seawater at 0°C (Castelli et al., 1974), and k_i is the temperature-dependent expression for pure ice from Sakatume and Seki (1978). The effective sea ice specific heat is from BL99

$$c = c_i + \frac{L\Gamma S}{T^2}, \tag{5}$$

where the first term is pure ice specific heat ($c_i = 2062$ J kg^{-1} K^{-1}) and the second one accounts for internal phase change, where $L = 335{,}000$ J kg^{-1} is the pure ice latent heat. The advection of heat by brine motion is neglected in the heat equation, which seems reasonable since the SIPL is isothermal.

2.1.2. Calculating New Ice Formation Assuming High Initial Liquid Fraction

A second key model aspect to platelet ice representation is the formation of new ice at the base of an existing sea ice cover. Under a net heat loss at the sea ice base, new ice forms in the model. New ice formation at the base converts seawater with salinity $S = S_w$ and $T = T_f$ (giving $\phi = 1$ according to Equation 3), into new sea ice, for which properties must be specified, in order to provide boundary conditions to the heat and salt transport equations.

The new ice temperature, T_{new}, is assumed to remain equal to T_f. The new ice bulk salinity, S_{new}, is that of unconsolidated platelet ice with porosity ϕ_{new}:

$$S_{new} = \phi_{new} S_w, \tag{6}$$

$$T_{new} = -\Gamma S_w, \tag{7}$$

where ϕ_{new}, the new ice porosity is an introduced model parameter, which must be higher or equal to the target unconsolidated platelet ice liquid fraction. We understand ϕ_{new} as the optimal porosity resulting from the competition between upward buoyancy forces tending to reduce *brine fraction* and the mechanical forces in the matrix of intertwined platelet ice crystals opposing the former. By contrast with Buffo et al. (2018), this force balance is not explicitly resolved by our model. Instead there is an instantaneous, prescribed change in liquid fraction from 1 to ϕ_{new}, which implicitly assumes a net salt loss from sea ice to the underlying ocean due to these processes. Turner et al. (2013) tested the sensitivity (SEN) of the predictions of a mushy layer model to such an ice-ocean interface liquid fraction, and showed that $\phi_{new} = 0.75$ provides a good fit to laboratory and young ice growth observations. Based on the field observations of Smedsrud and Skogseth (2006), Turner and Hunke (2015) later used $\phi_{new} = 0.75$ to represent newly formed frazil/grease ice, an ice type with similar liquid fraction to the unconsolidated platelet ice layer (Langhorne et al. (2015) and references therein). For all these reasons, we therefore set $\phi_{new} = 0.75$ in this paper, which we keep constant because the uncertainty in ϕ_{new} is relatively low (0.09 according to Langhorne et al. (2015)), compared with other model parameters.

The rate of change in ice thickness dh_i/dt due to new ice formation, follows from Schmidt et al. (2004):

$$\rho_i \frac{dh_i}{dt} = -\frac{F_w - F_c}{E_{new} - E_w},$$ (8)

where F_w and F_c are the oceanic sensible and ice conductive heat fluxes (both positive upwards), whereas $E_{new} = E_i(S_{new}, T_{new})$ and $E_w(S_w, T_f)$ are the specific enthalpies (J kg^{-1}) of new sea ice and source seawater, respectively. Expressions for the enthalpies of sea ice and seawater assume a reference (REF) energy zero-level at 0°C and are detailed in Schmidt et al. (2004) and Jutras et al. (2016). There are two features of platelet ice growth obvious from Equation 8. The first remarkable feature can be seen by considering the specific enthalpy difference $\Delta E = E_{new} - E_w$, which proves only dependent on ϕ_{new}. For example, $\Delta E = -82.6 \text{ kJ kg}^{-1}$ for $\phi_{new} = 75\%$, about three times smaller in magnitude than the typical value inferred for a new ice salinity of 6.8 g kg^{-1} of $\Delta E = -264.4 \text{ kJ kg}^{-1}$ for $\phi_{new} = 20\%$. This implies that the rate of increase in ice thickness for $\phi_{new} = 75\%$ is about three times as large as for $\phi_{new} = 20\%$. Second, since in platelet mode $F_w \gg F_C$ the rate of increase in ice thickness in the unconsolidated platelet mode is mostly driven by the ocean heat flux and is independent of ice thickness—in contrast to the columnar situation where ice growth rate varies as $1/h_i$ (Maykut, 1986). This implies that the thickness of unconsolidated platelet ice in the SIPL layer is limited by the length of the growth period, not by the ice thickness.

2.1.3. Introducing a Convective Gravity Drainage Parameterization

Once an unconsolidated platelet ice layer is formed, capturing salt dynamics is essential, as will be shown in Section 3. The SIPL is nearly isothermal (Hoppmann, Nicolaus, Paul, et al., 2015; Robinson et al., 2014). Because brine salinity and temperature are coupled through the liquidus relationship, the SIPL is also characterized by a vertically homogeneous brine salinity. Hence, diffusive parameterizations for gravity drainage are not appropriate because they are not able to transport salt in the absence of a brine salinity gradient. For this reason, we replaced the default diffusive parameterization of gravity drainage (Vancoppenolle et al., 2010) by the advective parameterization of GN1315.

The GN1315 gravity drainage parameterization mimics the features of brine circulation suggested by high-resolution simulations of fluid flow in growing sea ice (Wells et al., 2011). GN1315 assumes that the model sea ice layers lose brine mass through brine channels directly to the ocean. In response, an upwards return flow effectively desalinates the sea ice. Here we use the reformulation of Thomas et al. (2020) which is strictly equivalent to GN1315, and has a vertical upwelling velocity associated with the return flow, following Rees Jones and Worster (2014). In layer k, the vertical convection velocity is given by:

$$w_k = -\frac{\alpha}{\rho_{br}} \sum_{i=1}^{k} \max\left(\left[Ra_k - R_c \right], 0 \right) \Delta z_i$$ (9)
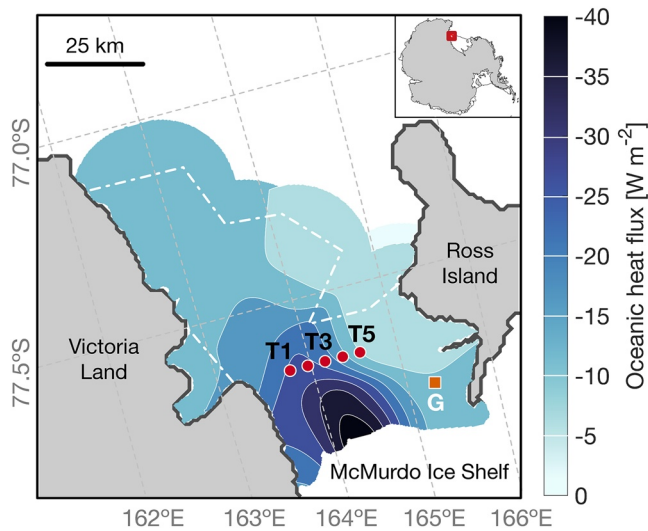
Figure 2. Map showing the McMurdo Sound region, and observational sites G and T1–T5 relevant to this study. Colored contours give the observation-based historical retrievals of the oceanic heat flux, corresponding to years 1966–2014 (Langhorne et al., 2015). Regions within the dash-dot contour have uncertainties on the oceanic heat flux smaller than 50%. Note that site G, with its observational time series, has a different symbol.

Table 1
Summary of Site G (77.78°S) Last Observed on October 1, 2009 (Gough, Mahoney, Langhorne, Williams, Robinson, et al., 2012) and Sites T1–T5 on the Transect (77.67°S) Visited on November 16, 2009 (Langhorne et al., 2015)

Site	Longitude	Mean snow thickness[a] (m)	Ice thickness[a] (m)	SIPL thickness[a] (m)	F_w (W m^{-2})
G	166.3°E	0.15	2.07	0.25	−6.0
T1	164.8°E	0.06	2.47	2.18–2.19	−20.7
T2	165.0°E	0.08	2.47	2.83–2.89	−21.2
T3	165.2°E	0.09	2.29	1.81–1.91	−18.1
T4	165.4°E	0.05	2.29	0.55–0.61	−11.8
T5	165.6°E	0.04	2.14	0.04	−5.2

Abbreviation: SIPL, sub-ice platelet layer.
[a]Mean snow thickness, ice thickness, and SIPL thickness at site G and sites T1–T5 were measured on October 1, and November 16, 2009, respectively.

where α is the gravity drainage strength parameter (in kg m^{-3} s^{-1}), ρ_{br} is brine density, Ra_k is the Rayleigh number in layer k, R_c is a critical Rayleigh number value, and Δz_i is the thickness of the ith model layer. Ra expresses the ratio of destabilizing buoyancy forces versus stabilizing forces, modulated by permeability (Notz & Worster, 2008):

$$Ra_k = \frac{g \Delta \rho \langle \Pi \rangle_z \left(z_k - h_i \right)}{\mu \kappa}, \qquad (10)$$

where g is gravity, $\Delta \rho$ is the brine density difference at position z in the ice, with respect to the base of the ice, $\langle \Pi \rangle_z$ is an effective measure of permeability at position z, μ is viscosity and κ is thermal diffusivity.

Wongpan et al. (2018) show the mean permeabilities of columnar and incorporated platelet ice are indistinguishable. Hence for both we use the formula of Freitag (1999), $\Pi = \Pi_0 \left(\phi \right)^{3.1}$, where $\Pi_0 = 1.995 \times 10^{-8}$ m^2, is the local permeability coefficient at depth z. The effective permeability between z and the bottom of the ice is characterized by the harmonic mean permeability, following Griewank and Notz (2015). Griewank and Notz (2015) used $R_c = 4.89$ and $\alpha = 5.84 \times 10^{-4}$ kg m^{-3} s^{-1} as values for their key tuning parameters.

2.1.4. Applying Appropriate Forcing at the Ice Base

The last required ingredient to produce unconsolidated platelet ice in the model is to apply an appropriate sensible heat loss from the ice base to the ocean below, which is done through a negative oceanic sensible heat flux F_w. F_w is a priori site- and time-dependent, and it is quite difficult to obtain direct measurements of F_w that are consistent with mass balance observations.

2.2. Simulation Protocol

2.2.1. Observational Framework

We use observations from 2009 at six different sites, located in the vicinity of the McMurdo Ice shelf (Figure 2): Site G—where a large set of year-round observations was acquired in 2009 (Gough, Mahoney, Langhorne, Williams, & Haskell, 2012, Gough, Mahoney, Langhorne, Williams, Robinson, et al., 2012); and five sites T1–T5, arranged along a transect line, where a few observations of the SIPL were taken on one instance, on November 16, 2009.

For logistical reasons site G was located on the east side of McMurdo Sound (77.7758°S, 166.3128°E, see Figure 2) close to New Zealand's Scott Base. This eastward location implies a rather thin SIPL (∼0.2 m in November 2009, Gough, Mahoney, Langhorne, Williams, Robinson, et al., 2012; Langhorne et al., 2015). Observations at site G include high temporal resolution temperature (every 10 min, from May 29 to November 19, 2009) and salinity profiles (every two weeks, from May to October 2009). Consolidated ice and SIPL thicknesses were also recorded, by drilling a hole through the ice cover, inserting a "T" bar, and pulling it upwards to record a minimal and maximum resistance. Snow depth was recorded using a ruler.

The T1–T5 sites were aligned along the 77.6667°S parallel, from 164.8°E to 165.6°E in 0.2° steps (see Table 1 for a summary description). Unlike

Table 2
Summary of Forcings Applied to the Model

Forcing	Unit	Method	Sources
Downwelling longwave radiation	W m^{-2}	Computed	Efimova (1961)
Shortwave radiation	W m^{-2}	Retrieved	NIWA[a]
Air temperature	K	Retrieved	NIWA
Atmosphere pressure	Pa	Retrieved	NIWA
Specific humidity	kg kg^{-1}	Retrieved	NIWA
Wind speed	m s^{-1}	Retrieved	NIWA
Cloudiness	–	Retrieved	AMRC[b]
Oceanic heat flux	W m^{-2}	Prescribed	Gough, Mahoney, Langhorne, Williams, Robinson, et al. (2012) and Langhorne et al. (2015)
Snowfall rate	m s^{-1}	Retrieved	Gough, Mahoney, Langhorne, Williams, Robinson, et al. (2012)
Albedo	–	Computed	Shine and Henderson-Sellers (1985)

[a]National Institute of Water and Atmospheric Research (https://cliflo.niwa.co.nz/). [b]The Antarctic Meteorological Research Center (http://amrc.ssec.wisc.edu/).

site G, these sites are in the path of the main outflow of ISW from the McMurdo Ice Shelf and hence comparatively have a much thicker SIPL (Hughes et al., 2014; Langhorne et al., 2015). Observations at the T sites include snow depth, ice and SIPL thickness on November 16 (Table 1).

2.2.2. Forcing and Initializing the Model

Most of the material presented in this paper are model simulations with LIM1D at G and T sites, forced by thermal forcing at the upper and lower interfaces. Simulations at different sites are identical in terms of surface forcing but differ in terms of oceanic heat flux. All simulations ran from April 2, 2009, when ice started to form (Gough, Mahoney, Langhorne, Williams, Robinson, et al., 2012), and we apply an initial 0.05 m thickness. Simulations stop at the last measurement date, October 14 at site G and November 16 at sites T1–T5.

Surface forcing includes atmospheric state, radiation fluxes and snowfall. For atmospheric state and downwelling solar radiation flux at the air--ice interface, we used Scott Base and McMurdo Station weather stations data archived by National Institute of Water and Atmospheric Research (NIWA) and the Antarctic Meteorological Research Center, see Table 2. Downwelling longwave radiation, sensible and latent heat fluxes were retrieved from observed air temperature, humidity, and cloudiness, using the parameterizations of Efimova (1961) and Jacobs (1978), as recommended in Vancoppenolle et al. (2011). The snowfall rate was derived from snow depth observations at G site (Gough, Mahoney, Langhorne, Williams, Robinson, et al., 2012) and applied to all G and T sites simulations.

The oceanic sensible heat flux is the most critical and the most uncertain forcing field. At site G, we have a time series of temperature profile and ice thickness from which F_w can be estimated in a time-dependent fashion (Gough, Mahoney, Langhorne, Williams, Robinson, et al., 2012). The assumptions made through these calculations are not entirely consistent with LIM1D thermodynamic formulations. Hence, at site G, instead of using the detail of the time-series, we force the model with a constant value of $F_w = -6$ W m^{-2}, in recognition of an uncertainty of ± 5 W m^{-2} within the observational calculation (Gough, Mahoney, Langhorne, Williams, Robinson, et al., 2012). This value of F_w is conservative compared to -13 W m^{-2} used as the ocean heat flux value for 2009 McMurdo Sound sea ice in the BL99-based modeling of Smith et al. (2015). By contrast, over the T1–T5 transect, we do not have detailed time series measurements of sensible oceanic heat input. However, the circulation-driven spatial pattern of ocean heat flux in McMurdo Sound is consistent from year to year (e.g., Dempsey et al., 2010; Langhorne et al., 2015). Using a very simple model to derive mean, late winter, ocean heat flux from approximately 100 observations collected between 1966 and 2014, Langhorne et al. (2015) have produced location-dependent values for F_w (see Figure 2). In the end we run 31

Table 3
Summarized Description of the Model Simulations Used in This Work. N_{runs} Refers to the Number of Simulations, F_w to the Ocean-To-Ice Sensible Heat Flux, N_{layers} to the Number of Vertical Layers

Description	Site	N_{runs}	Snowfall	F_w	N_{layers}	Figures	Free parameters[a]
Reference experiments (REF, G & T sites)							
REF, Standard snowfall	G	1	ref	−6	50	6,7	Ref
	T1–T5	31	ref	[0, −30]	50	4,5,8–10, S1	Ref
REF, Perturbed snowfall	T1–T5	62	× 0.5, × 2	[0, −30]	50	8	Ref
Sensitivity experiments (SEN, T3 site)							
SEN, ϕ_{new} and salt advection	T3	3	ref	−18	50	9	Ref
SEN, Number of layers	T3	2	ref	−18	3,10	10	Ref
SEN, Free parameters	T3	33	ref	−18	50	S2, S3, S4	Perturbed

[a]Reference values for free parameters: $k_s = 0.31$ W m^{-1}K^{-1}, $\alpha = 5.84 \times 10^{-4}$ kg m^{-3}s^{-1}, $R_c = 4.89$.

simulations, holding F_w constant in time but spanning the observational range (0−−30 Wm^{-2}) in increments of 1 Wm^{-2}. We label T1–T5 the subset of these simulations for which F_w value matches the observational retrieval (see last column of Table 1)

All forcings are interpolated to the model time step. Unless otherwise noted, we used one layer of snow, 50 layers of sea ice and a time step of 10 min, which ensures numerical stability of the salt advection explicit scheme. Numerical stability was verified using a Courant-Friedrichs-Lewy criterion (Courant et al., 1967), calculated with the maximum vertical velocity (Figure S1). Additional quality control tests confirmed that energy and salt are conserved sufficiently accurately for our purposes (Figure S1).

Our forcing and tuning strategy differs from that of Buffo et al. (2018), who modeled platelet ice formation in a region with similar sea ice phenomena. As model forcings, they apply an idealized surface temperature time series and ocean supercooling, which was tuned to achieve a realistic incorporated platelet ice thickness at the end of the growth season. By contrast, we apply observational estimates of atmospheric and oceanic heat fluxes and use standard values for free parameters (snow thermal conductivity and gravity drainage parameters). In the discussion (Section 4.2) we will come back to the possible reasons to explain why the Buffo model rarely simulates an SIPL.

2.2.3. Simulations

Among the simulations conducted for this study (Table 3), let us first mention our REF simulations. These are a series of 31 model experiments, each performed with a given value of the sensible ocean-to-ice heat flux F_w, corresponding to a set of location-dependent observational estimates. The manual evaluation consisted in comparing observations to model output, from the subset of six simulations corresponding to the appropriate values of F_w at the G and T sites. The resulting REF experiments are described in Section 3.1. The REF simulations have been also performed with half and double snowfall.

In addition, several series of SEN runs were performed, all at site T3. A first series highlight the respective role of new ice formation and advective desalination on the formation of an SIPL. In the first of these simulations the new ice porosity is set to 25% (instead of 75% in the REF); in the second, brine convection is turned off, and in the third both changes are applied in concert.

In another series of SEN simulations, the number of vertical layers in the ice was varied. A final series of SEN experiments targeted the role of what we consider as free parameters, namely apparent snow thermal conductivity, critical Rayleigh number and gravity drainage strength parameter (Figures S2, S3, and S4). We describe these in more detail here as these experiments decided the final retained value of free parameters.

The apparent snow thermal conductivity k_s is deemed uncertain because it encompasses several, not all resolved, heat transfer processes: the conduction of heat by ice crystals and air within the snow, the advection of heat by wind pumping and the transfer of latent heat due to sublimation of snow crystals. Increasing
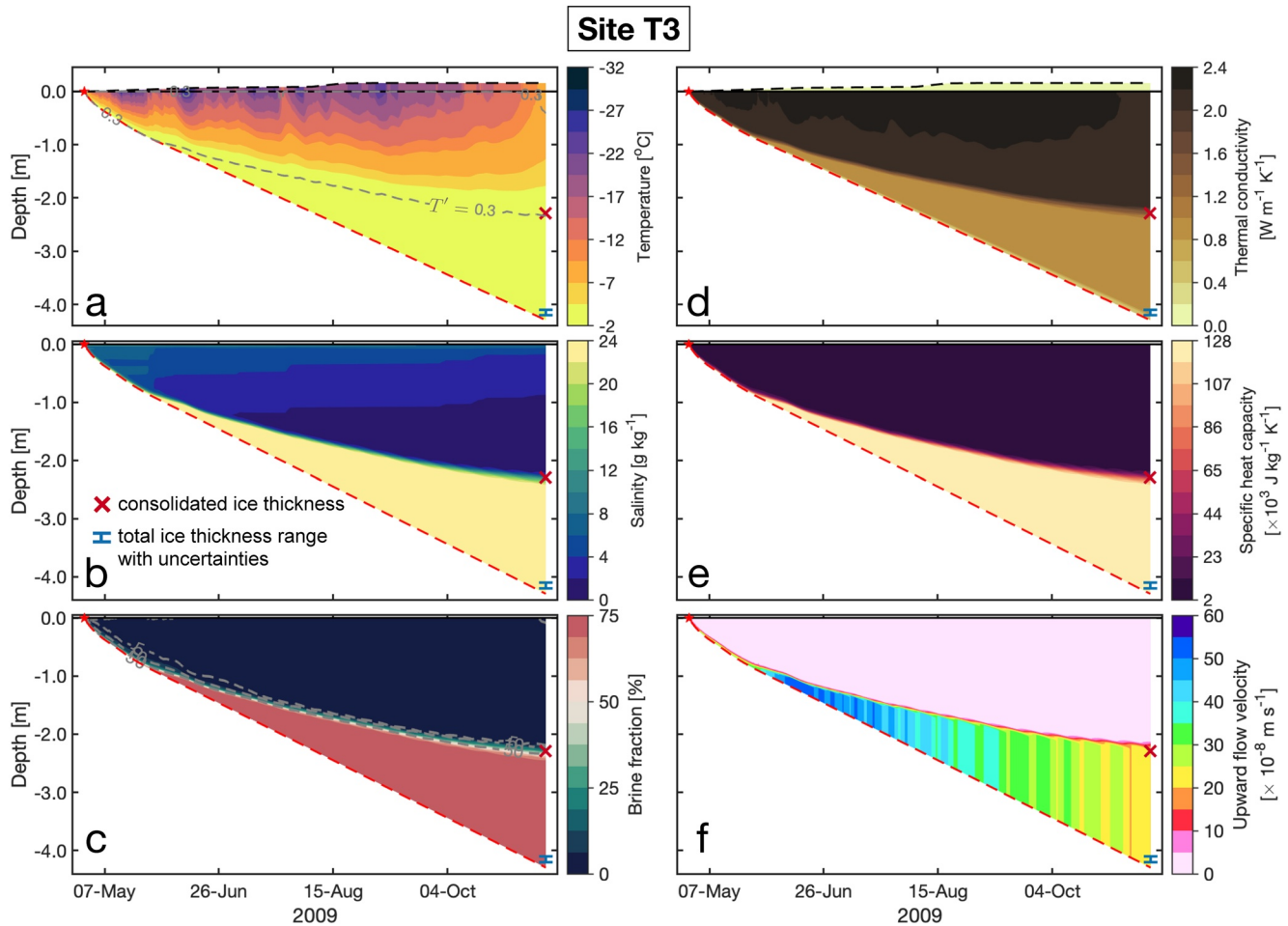
Figure 3. Evolution of sea ice thermohaline properties, contoured in the sea ice domain, at the site T3: (a) temperature, (b) bulk salinity, (c) brine fraction, (d) thermal conductivity, (e) effective specific heat capacity, and (f) upward brine Darcy velocity. Symbols refer to observed consolidated ice thickness (red "x") and sub-ice platelet layer positions (blue "I"). Red-dashed lines represent total ice thickness. Note that T' in (a) is temperature gradient (°C m^{-1}). Simulations using $F_w = -18$ Wm^{-2} (Table 1) and reference parameters of Table 3.

snow thermal conductivity enhances heat transfer in the snow-ice system (e.g., Lecomte et al., 2013), cooling and thickening the consolidated ice by ~30 cm when changing k_s from 0.2 to 0.7 W m^{-1}K^{-1}. Increasing k_s also thins the SIPL by about the same amount (Figure S2). In our REF simulations (Table 3), we use the standard value of $k_s = 0.31$ W m^{-1} K^{-1}.

The gravity drainage parameters–gravity drainage strength parameter (α) and critical Rayleigh number (R_c) – control the convection of brine during growth and influence the vertical salinity profile. Using standard values from Griewank and Notz (2015), as ultimately done in our REF experiments, gives best agreement with observed ice salinity profiles times series at site G (see Section 3). This is no surprise since these were tuned against young artificial sea ice salinity profiles, with similar physics to the consolidated ice observed at site G. Their influence on ice and SIPL thickness is low over a wide SEN range (see Figures S3 and S4).

3. Results

In the extensive set of simulations that was performed, an SIPL with varying thickness was detected in many instances. A typical well-developed SIPL can be seen in Figure 3, where the evolution of the simulated sea ice thermohaline properties is given for the REF simulation with the value of F_w that is appropriate for site T3. In other instances, no SIPL or a very thin one develops, and regular consolidated ice is simulated, such as at site G.
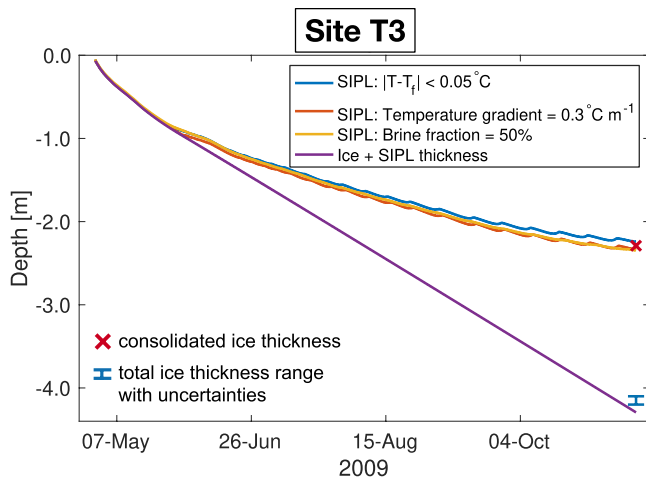
Figure 4. Sub-ice platelet layer diagnostics at site T3 with three different criteria ($|T - T_f| < 0.05°C$), temperature gradient = $0.3°C\,m^{-1}$, brine fraction = 50%). Note that $N = 50$ layers (see Section 3 for details).

The model SIPL can be identified as a highly porous region located directly above the bottom of the ice (with brine fraction close to $\phi_{new} = 75\%$). It is also characterized by vertically constant thermohaline properties: temperature is close to freezing (as reported by Robinson et al., 2014), and bulk salinity is approximately ϕ_{new} times seawater salinity (here ~25.5 g kg^{-1} in Figure 3b). Above the SIPL, temperature and salinity are similar to what is observed and typically simulated in regular congelation ice, such as at site G.

We tested three possible definitions of the upper SIPL boundary (Figure 4), using the contours of (a) $|T - T_f| = 0.05°C$, (b) 50% brine fraction and of (c) $0.3°C\,m^{-1}$ temperature gradient. All of them give meaningful and consistent estimates of the upper boundary of the SIPL.

In the following section, we first describe the evaluation of model simulations with observations (Section 3.1). We then focus on the simulated SIPL and the associated mechanisms: the thermal stabilization of the SIPL by large liquid fraction (Section 3.2), salt transport processes (Section 3.3) and their coupling with thermal processes (Section 3.4).

3.1. Evaluation of the Model With Observations

The model simulations capture nearly all available measurements performed at G and T sites within uncertainty range.

First, our simulations reproduce the time evolution of the sea ice cover. Simulated temperature profiles are mostly linear and, at G site, where observations are available, generally agree with observations (Figures 5b
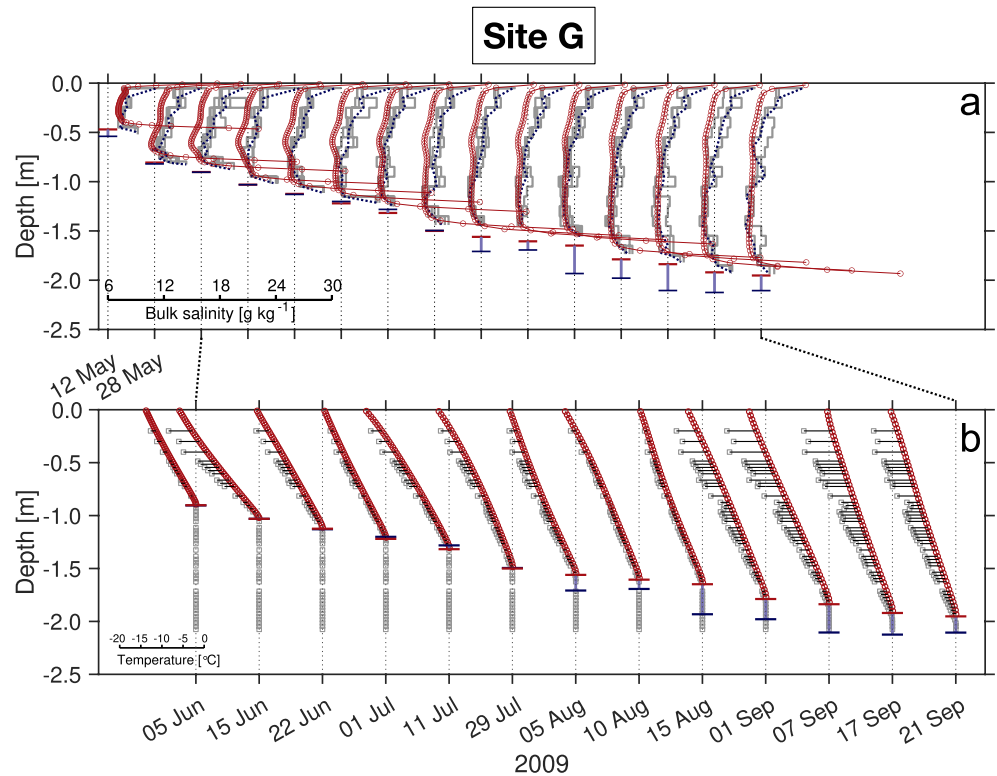

Figure 5. Simulated (red) and observed (gray) time series of salinity and temperature profiles at site G, (a and b) for $F_w = -6\,Wm^{-2}$ and reference parameters of Table 3. Horizontal red and blue bars represent the total ice thicknesses from simulations and observations, respectively.
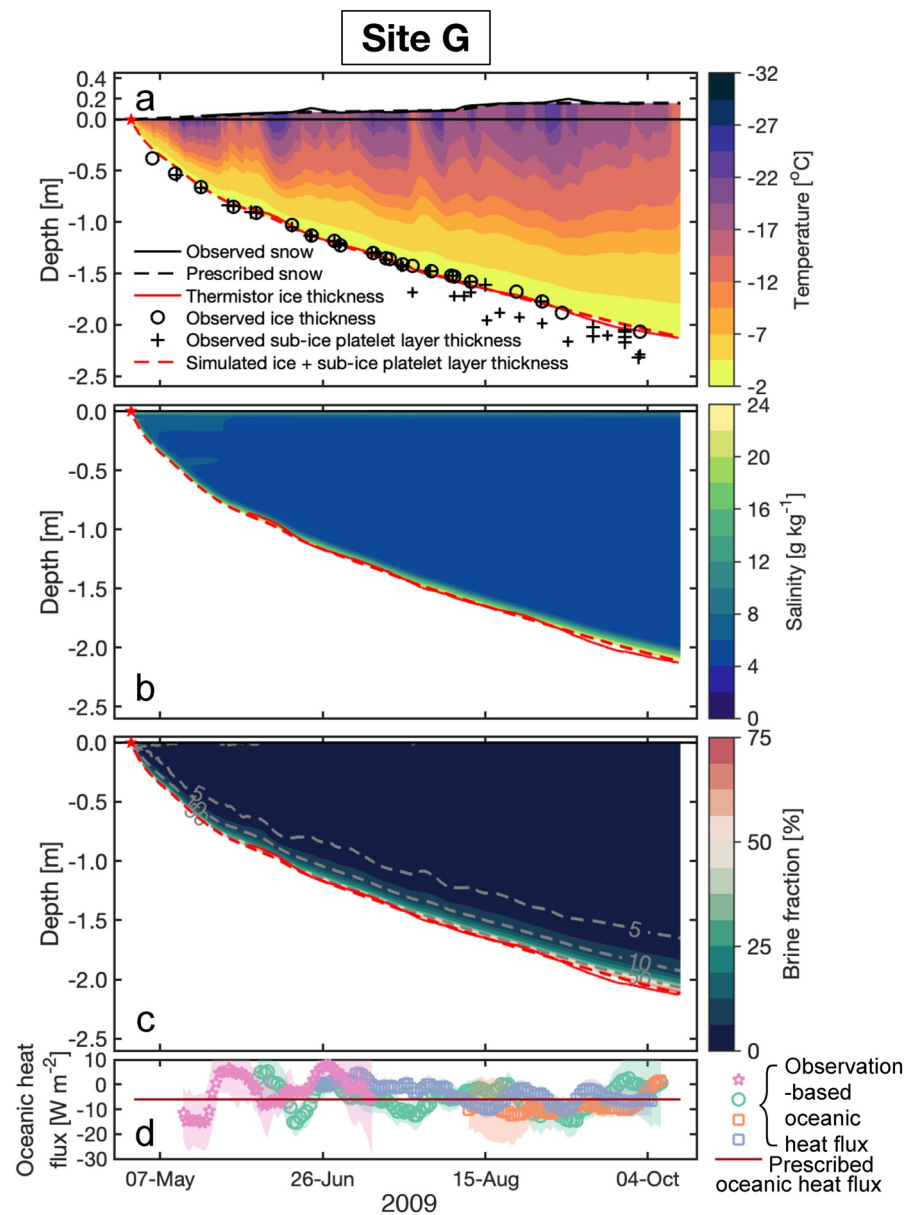
Figure 6. Evolution of sea ice thermohaline properties, contoured in the sea ice domain, at site G: (a) temperature, (b) bulk salinity, (c) brine fraction using reference parameters of Table 3. The d panel depicts time series of the oceanic heat flux as retrieved from thermistor string observations (symbols; Gough, Mahoney, Langhorne, Williams, Robinson, et al., 2012); along with the constant value applied as model forcing (red line) of $F_w = -6$ Wm^{-2}.

and 6a). Simulated temperature is warmer than observed in September due to unidentified model or forcing errors. The simulated salinity profile within the consolidated ice exhibits the typical C-shape (Figures 5a and 6b), in agreement with observations, with a systematic but low near-surface bias. The simulated consolidated ice thickness at site G is within a few centimeters of the observed value. Using an observation-derived, long-term oceanic heat flux of $F_w = -6$ Wm^{-2} (see Figure 2), our simulations do not capture the relatively thin SIPL (~0.20 m) observed at site G. However, within the context of largely uncertain and influential oceanic heat flux, the SIPL at site G represents a low amount of heat and is variable among the different observation methods (see symbols in Figures 6 and Figure 7b).

The second important quality of our model simulations is that they reproduce the observed spatial variations in consolidated ice and SIPL thicknesses. Indeed, the model faithfully reproduces the nearly linear
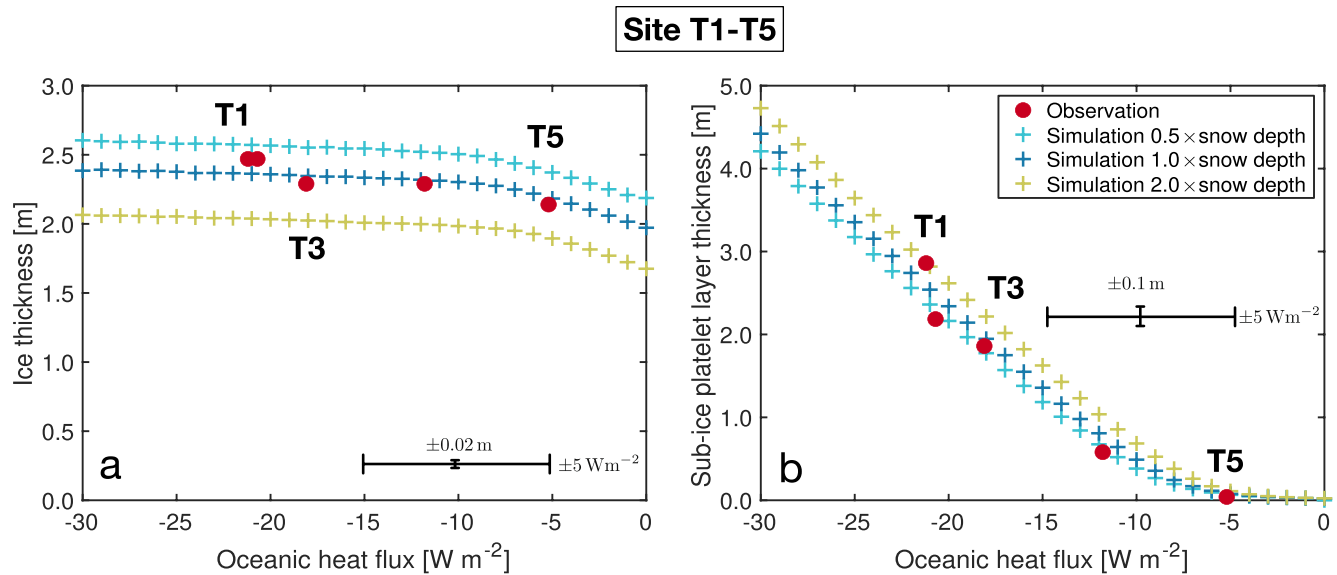
Figure 7. Simulated and observed (a) total ice thickness and (b) sub-ice platelet layer (SIPL) thickness against sensible oceanic heat fluxes with three snow-depth sensitivities (half, observed, and double). Oceanic heat fluxes are the observation-derived long-term means from Langhorne et al. (2015), applied as forcings to model simulations. Thicknesses correspond to model and observational values at T sites on November 19, 2009. Model SIPL thickness is diagnosed from the depth difference between the 50% brine fraction contour and the base of the ice. Measurement uncertainties in thicknesses and oceanic heat fluxes are shown as a single error bar on each plot (black lines).

response of the SIPL thickness to the oceanic heat flux at the T sites (Figure 8). Above $F_w \sim -5$ Wm^{-2}, no SIPL is simulated (see Figure 7), as observed at sites T5 and G. At the other extremity of the range, the SIPL thickness reaches around 3 m for $F_w \sim -20$ Wm^{-2}, as observed at site T1.

The observed relationship between SIPL thickness and F_w reflects a threshold competition between F_w and inner heat conduction flux (Dempsey et al., 2010; Gough, Mahoney, Langhorne, Williams, Robinson, et al., 2012). Above $F_w = -5$ Wm^{-2}, heat conduction is enough to compete with F_w and consolidates the newly formed ice, which corresponds to the classical case. Below -5 Wm^{-2}, heat conduction is insufficient to consolidate the ice. Once an SIPL is established, the conductive heat flux within the SIPL nearly vanishes, hence the SIPL growth rate becomes directly proportional to the oceanic heat flux. The consolidated ice thickness also increases with a decrease in F_w, but less so, because the rate of consolidation is ultimately determined by heat conduction above the SIPL, toward the atmosphere. In summary, the largely uncertain oceanic heat flux provides primary control on the SIPL thickness: a change in 5 Wm^{-2} in F_w typically corresponds to a difference in the SIPL thickness from 0.5 to 1 m.

Along with oceanic heat flux, snow accumulation is an influential and largely uncertain forcing field, as it controls heat conduction and the rate of consolidation. This is illustrated in Figure 7, where changes in simulated SIPL induced by several perturbations to snowfall are depicted. Increasing snow accumulation by a factor of 2 typically increases the SIPL thickness by 50 cm. Indeed, deep snow is more insulating than thin snow, which reduces the conductive heat losses and hence the means to consolidate the new ice forming at the base.

3.2. Thermal Stabilization of the SIPL by the Large Liquid Fraction

Since our simulations capture most of the observed behavior, it is legitimate to examine the mechanisms of SIPL formation and stabilization in the model, that mostly arise because of its large liquid fraction.

In all of our simulations, the SIPL develops once the conductive heat flux through the sea ice is too small to internally freeze the highly porous, newly formed ice. As the conductive heat flux decreases with an increase in ice thickness and snow depth, larger values of ice and snow thickness promote an SIPL. At site T3, for example, this occurs once the ice is about 1 m thick, in early June (see Figure 3).
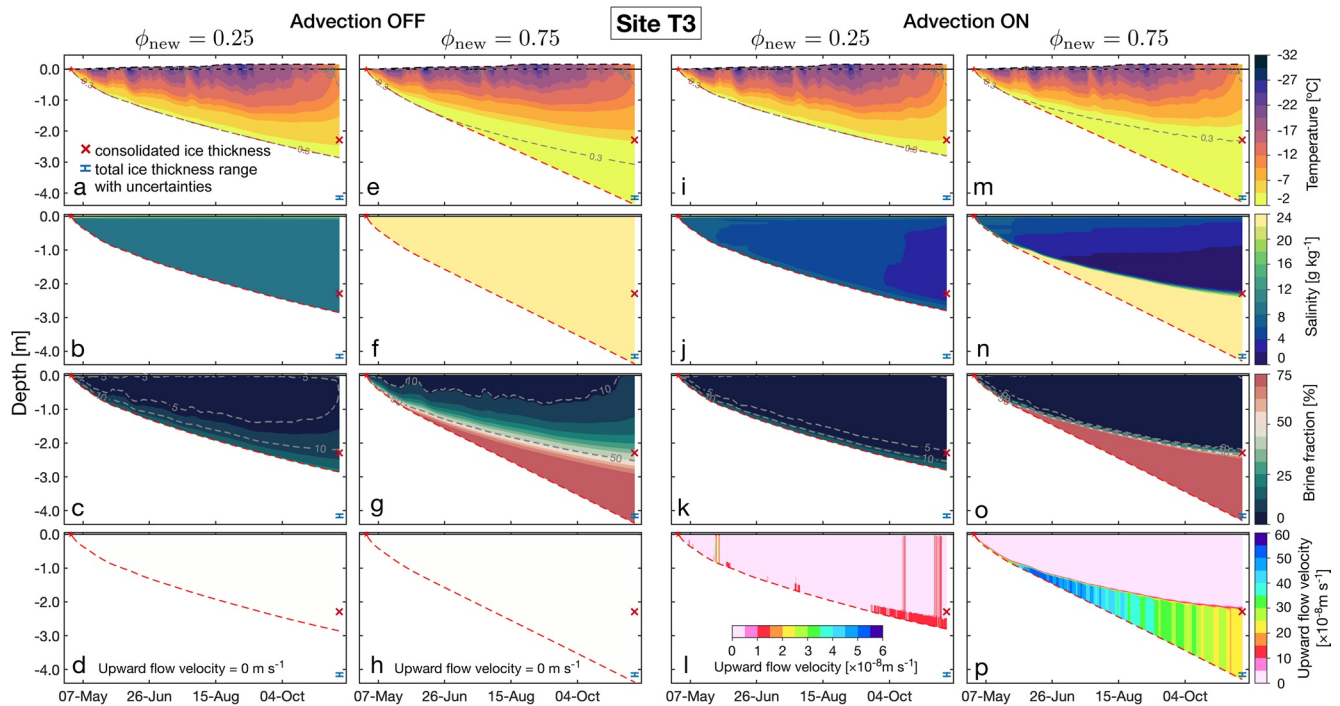
Figure 8. Influence of salt advection and initial brine fraction (ϕ_{new}) on sea ice properties. Namely, the evolution of temperature, salinity, brine fraction, and upward flow velocity contours in the sea ice domain, is given at site T3 from the four dedicated factorial simulations (see Section 2.4): (a–d) no salt advection and 25% initial brine fraction (e–h) no salt advection and $\phi_{new} = 75\%$ (i–l) salt advection and 25% initial brine fraction and (m–p) the REF experiment for which salt advection is activated and 75% for initial brine fraction is used. Symbols (red "x" and blue "range with uncertainties" "I") give consolidated and total ice thicknesses at site T3 on November 16, 2019. Red-dashed lines give simulated total ice thickness.

The thermal properties of the model SIPL (see Figures 3d–3f) are quite unusual as compared with those of typical sea ice, and mostly relate to the large brine fraction. First, the effective specific heat capacity (c_p) in the SIPL is close to 100 kJ kg^{-1} K^{-1}, one to two orders of magnitude larger than that of pure ice–mostly due to the latent heat term, reflecting the very large energetic cost of internal freezing at large liquid fraction. Second, the large liquid fraction lowers the thermal conductivity (k) down to ~1 W m^{-1} K^{-1}, about half of typical sea ice values (Pringle et al., 2007). Both c_p and k drastically reduce the thermal diffusivity of the SIPL as compared with typical congelation ice. In turn, the very low thermal diffusivity inhibits the development of a downward temperature gradient that would cool and reduce brine fraction in the SIPL. Overall, this chain of processes constitutes a stabilizing feedback for the SIPL. Above the SIPL, a thin transition layer toward more classical consolidated ice is simulated.

3.3. Haline Processes

In the presence of a well-developed SIPL, such as in the REF simulation at site T3 (Figure 3), the simulated convection system in congelation ice seems unaffected by the SIPL. The Rayleigh number (not shown) which controls the intensity of brine convection, features as for typical growing sea ice with a maximum at the base of the consolidated ice due to the combination of a relatively large permeability and a non-zero temperature gradient. The convective velocity rapidly increases near the base of the consolidated ice. By contrast, the SIPL is characterized by intense, vertically uniform convection (see Figure 3f), continuing the convection system from the congelation ice above. Time-dependent variations in the magnitude of the convective velocity in Figure 3f arise because the Rayleigh number increases as growth-driven buoyancy increases up to the critical value, whereupon overturning occurs with a commensurate drop in Rayleigh number (see Equations 9 and 10). Because the SIPL is isothermal, and therefore characterized by vertically constant brine salinity, such convection is inefficient at changing bulk salinity and brine fraction in the

SIPL. The analysis above indicates that brine convection in the simulated SIPL is intense, but barely affects the congelation ice.

3.4. Coupled Thermo-Haline Processes

Which of thermal or haline processes trigger the SIPL development? What is their respective role? It is with this question in mind that we performed the factorial simulations for which the new ice porosity was reduced to 25% and/or salt advection was deactivated. These simulations are described in Section 2.2.3 and Table 3. Their results are summarized in Figure 8.

Simulations suggest that a large (75%) initial liquid fraction is necessary to SIPL formation, whereas salt advection is not. When a large (75%) initial brine fraction is used, regardless of the activation of salt advection, an SIPL develops, as can be seen from brine fraction contours (panels g and o in Figure 8).

Active haline processes add two important features. First, they govern the expected and essential desalination of the consolidated ice, decreasing bulk salinity toward typically observed values. Second, the resulting loss of salt in consolidated ice sharpens the brine fraction contrast between the SIPL and the congelation ice. Without salt advection, the SIPL-congelation ice boundary is more gradual and spans a few tenths of centimeters (compare Figure 8 panels g and o). With salt advection, the vertical span of this boundary layer is of a few centimeters at most.

4. Discussion

Here we first review the plausibility of the simulated SIPLs (Section 4.1). Then, in Section 4.2, we discuss which key model features enabled its representation and why such SIPLs may not have been seen in previous model studies. Section 4.3 details what new understanding is brought by our analyses, and finally the limitations and research perspectives are discussed in Section 4.4.

4.1. How Realistic Is the Model SIPL?

The definitions of the boundaries of the SIPL are quite different in the modeling and observational worlds, yet the SIPL thickness agrees reasonably well between the two worlds (see Figure 4). This is because the model and observational definitions are not totally disconnected and were adjusted to be consistent. The first definition (see Figure 4), based on the difference in temperature from the freezing point, is difficult to achieve in field observations because very accurate measurement of salinity is needed just beneath the sea ice. In contrast the second diagnostic method, the 50% brine fraction contour, targets the structural weakening that is used in the observational "T-bar" method of Gough, Mahoney, Langhorne, Williams, Robinson, et al. (2012). In this method, the SIPL base is identified from a weak resistance when pulling a "T" bar upwards, whereas the consolidated ice base is identified when the "T" bar cannot be pulled further. Laboratory observations indicate that for brine fractions above 50%, an ice-liquid mixture can be stirred, whereas cohesion prevents stirring below that limit (Jutras et al., 2016). Hence, we conjecture that the change in internal cohesion identified from the T-bar method roughly corresponds to the 50% brine fraction limit. The third method identifies the SIPL from model output based upon the 0.3°C m^{-1} temperature-gradient. It targets the steep change in temperature with depth immediately above the SIPL, as observed in situ by Gough, Mahoney, Langhorne, Williams, Robinson, et al. (2012).

The simulated SIPL analogs can be deemed "realistic", in terms of physical properties, mechanisms of formation, and response to thermal forcing, giving the model some predictive capacity. The observational and the model worlds share many similarities. (a) The model SIPL is a highly porous layer, with vertically homogeneous thermohaline properties (temperature, brine fraction, bulk salinity), that is found below rather thick regular consolidated ice (see Figure 3). Porosity (or brine fraction) is about 75%, as a result of the prescribed value for initial brine fraction. Indeed, when using $\phi_{new} = 0.25$, the simulated SIPL disappears (see Figures 8i–8l for an example at T3 site). Temperature in the SIPL is very close to the freezing point, as observed (Gough, Mahoney, Langhorne, Williams, Robinson, et al., 2012; Robinson et al., 2014). Thermal equilibrium and the liquidus relationship impose brine salinities nearly equal to seawater values, forcing bulk salinities of about 75% of seawater. (b) The formation of the SIPL begins once the conductive heat

flux is no longer sufficient to reduce the SIPL brine fraction. The model confirms the postulate of Dempsey et al., (2010) and Gough, Mahoney, Langhorne, Williams, Robinson, et al. (2012) that this occurs when there is sufficient thermal insulation, that is, when ice and snow are thick enough. Further the peculiar thermal properties of the SIPL, a large effective specific heat capacity (Figure 3e) and a low thermal conductivity (Figure 3d), contribute to stabilize the SIPL by inhibiting temperature changes. (c) The linear response of the thickness of the model SIPL to oceanic heat flux forcing is comparable to what is understood from observations (Langhorne et al., 2015; Smith et al., 2012). In particular, the model acquires some predictive capacity for the SIPL thickness at the sites T1–T5 (Figure 7b), and retains its positive features with regard to the properties of columnar and incorporated platelet ice, in particular those observed at site G (Figure 5).

4.2. What Enables the Emergence of an SIPL in the Model World?

Next to specifying realistic atmospheric and oceanic forcing fields, several model features were found to be essential for the emergence of a realistic SIPL. These mostly relate to the representation of brine, now central in sea ice thermodynamic models following developments over the last 30 years (Worster, 1992; BL99; Vancoppenolle et al., 2010; Hunke et al., 2011; GN1315; Rees Jones & Worster, 2014).

Specifying an initially large brine fraction is a prerequisite that can only be implemented if salt dynamics are considered. The key contribution of the salt dynamics is to contrast the large bulk salinity and brine fraction within the SIPL with lower values in the consolidated ice. Without salt dynamics, high initial brine fraction would lead to unrealistically large bulk salinities throughout the ice (see Figures 8f and 8g). A consistent connection between brine fraction and thermal properties gives the SIPL its rather low thermal diffusivity and its thermodynamically stable character. Because they either partially or fully neglect these characteristics, sea ice models of the previous generations (Semtner, 1976; BL99) are insufficient to generate an SIPL. Such models do not represent salt advection and implicitly assume a low liquid fraction in new ice, via a specification of an initially low bulk salinity at the ice base, which corresponds to the left panels (a–d) of Figure 8. Such models cannot be fixed just by using $\phi_{new} = 0.75$ since then the salinity of congelation ice becomes unrealistically large (Figure 8f).

It is also worth discussing why an SIPL is a prominent feature of our simulations, whereas it was only rarely observed in the simulations of Buffo et al. (2018), despite the fact that they also used a mushy-layer approach. Let us first review the differences in model and experimental setup between the two studies. The representation of sea ice processes is quite similar in both models: mushy-layer thermodynamics, convective gravity drainage following GN1315 and a critical value for the initial liquid fraction in the sea ice system (0.7 for Buffo et al. (2018), 0.75 for this work). The model of Buffo et al. (2018) unusually departs from classical mushy-layer approaches, in that brine and pure ice are not in thermal equilibrium, which may explain why their brine salinity profiles are quite unusual. However, it is difficult to see how such differences would lead to large differences in terms of simulated SIPL.

One difference between the two studies is the version of the gravity drainage parameterization. Buffo et al. (2018) follow Griewank and Notz (2013), taking the effective permeability as the vertical minimum and 1.56×10^{-3} kg m^{-3}s^{-1} for the gravity drainage strength parameter. By contrast, we follow Griewank and Notz (2015), as recommended by Thomas et al. (2020), and use the harmonic mean permeability as the effective value and the corresponding value of the gravity drainage strength coefficient (5.84×10^{-4} kg m^{-3} s^{-1}). However, our supplementary analysis suggests (Figures S3 & S4), that such a difference in gravity drainage is unlikely to generate large differences in SIPL thickness and properties.

Within the water column, the Buffo et al. (2018) model is more detailed than ours. In particular, their model domain includes the water column, whereas our model domain only includes sea ice (defined as the depths where liquid fraction is less than one). Their ocean forcing is supercooling, from which they derive a nucleation rate. From a force balance, they calculate a solid fraction flux at the ice base. By contrast, we bypass this step and force our model at the base of the ice cover with prescribed ocean heat flux from which a sea ice mass accretion rate is calculated.

In terms of how heat exchanges with the atmosphere are represented, the Buffo et al. (2018) model is less general than ours. Two aspects deserve mention. First, we consider snow, they do not, and we find snow to be an important factor. Second, Buffo et al. (2018) use an idealized surface temperature time series as a

surface forcing. By contrast, we represent all components of the surface energy budget, and specify them as closely as possible to those observed in situ. The differences in the representation of snow and the surface energy balance probably lead to large differences in simulated heat conduction fluxes between the two models, which is key to SIPL growth.

The model forcing and tuning strategies are also quite different between the two studies. We did not tune parameters but applied the published and widely used values of snow thermal conductivity, critical Rayleigh number and gravity drainage strength parameter, driving our model with observationally constrained ocean and atmospheric heat forcing. We evaluated against several observables at different sites (consolidated ice thickness, ice salinity and temperature profiles, SIPL thickness). In the Buffo et al. (2018) study, model forcing (supercooling) is used for tuning, and only the incorporated platelet ice thickness at the time of sampling of the sea ice cores was considered as a tuning target. Such a strategy may lead, over the whole season, to significant errors in the energetics of the ice system, in particular in terms of the respective role of atmospheric and oceanic heat losses.

In conclusion, we surmise that it is a combination of these differences that leads to the almost complete absence of an SIPL in the Buffo et al. (2018) simulations. The three key elements responsible for this absence are that: (a) the SIPL was not actively sought, (b) the insulating role of snow was not considered, and (c) the tuning strategy allowed for compensation of errors in atmospheric heat fluxes by adjusting the oceanic heat sink.

4.3. Insight into Sub-Ice Platelet Layer Formation Mechanisms From Simulations

The phenology of the SIPL is generally well described in terms of thickness, seasonality and properties. The known processes relevant to the formation of the SIPL are summarized in Hoppmann et al. (2020). They include the formation of ISW from the basal melting of ice shelves, its ascent and the appearance of frazil crystals sometime after the ISW is in situ supercooled; the drift, rise and accumulation of frazil crystals at the base of the existing sea ice. An SIPL develops once platelet growth exceeds incorporation, which occurs for a sufficient flux of frazil crystals and sufficiently low conduction of heat (Dempsey et al., 2010; Gough, Mahoney, Langhorne, Williams, Robinson, et al., 2012). Less is known about the thermodynamic mechanisms that explain the stability, properties and fate of the SIPL once the ice crystals are available. One of the key contributions of the present paper is to propose mechanisms that fill in this gap, based on a standard description of sea ice halo-thermodynamics.

We provide insights on three elements key to the physics of the SIPL: (a) an accumulation of highly porous sea ice occurs when there is low heat conduction in the ice and a heat loss from the sea ice to the ocean; (b) large brine fractions thermally stabilize the SIPL as a vertically homogeneous layer; (c) salt transport sharpens the porosity contrast between the SIPL and the consolidated ice located above.

(i) The model SIPL starts forming when the heat conduction flux at the base of the ice is insufficient to internally freeze the highly porous new ice that keeps on forming because of the large oceanic heat loss. When such platelet conditions are met, newly formed ice with large brine fraction cannot freeze further and remains highly porous. In the model, such conditions are met when the ice is sufficiently thick (between 1.5 and 2 m), and snow depth reinforces insulating properties of the cover. Consequently, deep snow induces earlier formation of an SIPL.

(ii) The large liquid fraction provides the SIPL with thermal properties that contribute to its stability. Let us first mention the large effective specific heat capacity—up to two orders of magnitude larger in the SIPL than for ordinary ice—and thermal conductivity, twice as low in the SIPL as in consolidated sea ice, explaining the response of the SIPL to cyclic heating observed by Hoppmann, Nicolaus, Hunkeler, et al. (2015). In turn, the low thermal diffusivity inhibits temperature changes, producing a vertically homogeneous temperature profile. The lack of vertical temperature gradient prevents the internal freezing of the SIPL.

(iii) No temperature gradient within the SIPL also means no brine salinity gradient (because of thermal equilibrium). Therefore, liquid convection, which is simulated to be the most intense in the SIPL, as expected (Robinson et al., 2014), appears to be inefficient at desalinating the SIPL in our model with a quiescent ocean beneath. This contributes to preserving large liquid fractions in the SIPL and reinforces
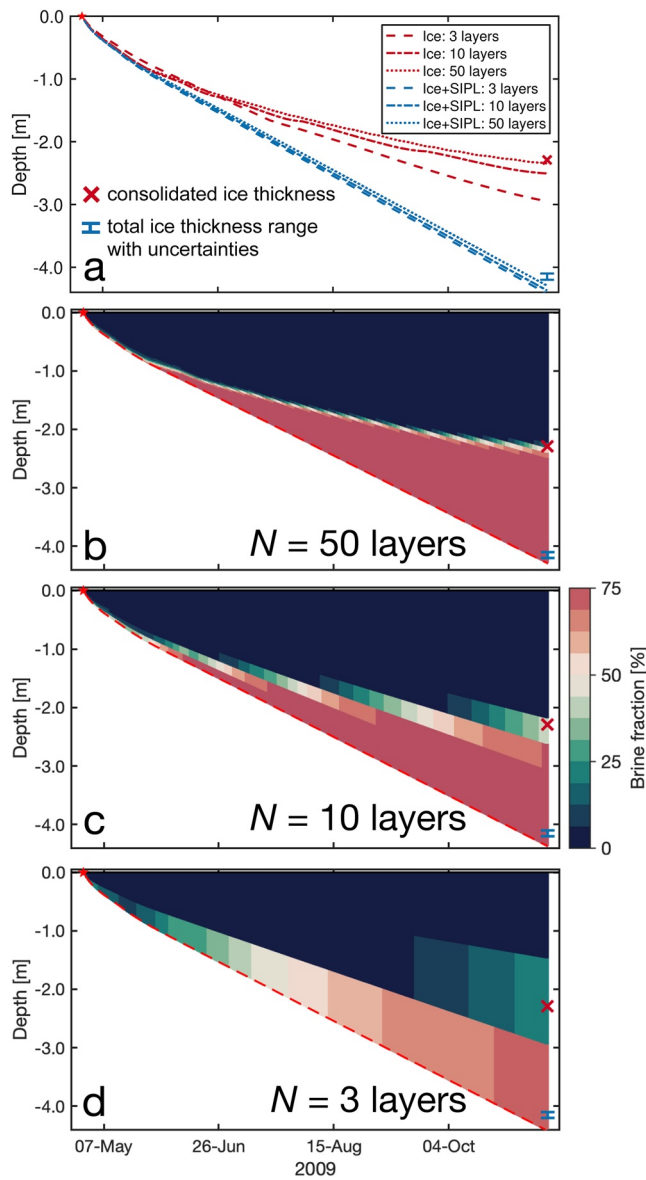
Figure 9. Sensitivity to vertical resolution of (a) sub-ice platelet layer thickness (diagnosed using 50% brine fraction); (b–d) brine fraction contours for 50, 10 and 3 layers, respectively.

the thermal stabilization of the SIPL. By contrast, in the consolidated ice above the SIPL, the temperature gradient generates desalination. For these reasons, brine convection generates a structural contrast between the SIPL and consolidated ice.

Peculiar features of SIPL growth rate are also explained by our model. First, because of the high liquid fraction, the SIPL grows much faster (approximately three times as fast because ϕ_{new} = 75%) than classical congelation ice, which is characterized by lower liquid fractions. Second, platelet ice growth is linearly related to thermal forcing (as observed by e.g., Smith et al., 2012). This is unlike congelation ice for which the growth rate decreases with ice thickness (Maykut, 1986), eventually reaching a limiting thickness. These features suggest the continuous growth of an SIPL as long as forcing is sustained, which explains the large SIPL thicknesses observed in nature (Hoppmann, Nicolaus, Hunkeler, et al., 2015; Hughes et al., 2014).

4.4. Use in Large-Scale Investigations: Perspectives and Limitations

The numerical cost, which is tightly linked to the number of vertical layers required to simulate the SIPL, is one of the concerns for the future implementation of our approach into large-scale models. To provide insight on this matter, the SEN of the simulated SIPL to the number of vertical layers was tested by decreasing the number of layers from 50 to 10 and three layers (Figure 9). We found that a physically consistent SIPL emerges with moderate accuracy in thickness for N = 3 layers. Increasing the number of layers (we ran up to 200 layers) thickens the SIPL by moving its upper boundary upwards, so that it ultimately coincides with the temperature inflection. The exact location of the SIPL, taken as the 50% brine fraction contour, is set by the width of the salinity transition. The latter sharpens with more layers, but keeps spanning 3–5 layers, with a similar structure centered around the temperature inflection regardless of resolution. As there are no physical means in the model to transport salt without a temperature gradient, the salinity transition (and the SIPL exact location) is set by numerical diffusion of the salt advection and vertical remapping schemes. With 10 layers, the position of the SIPL is reasonably captured.

Several limitations in our understanding remain, restricting our current capabilities to predict the occurrence of the SIPL and its properties. We consider water column processes in general and the liquid convection in the SIPL as two remaining major sources of uncertainty.

Water column processes were out of the scope of this study. Still, the development of an SIPL in our simulations depends to first order on the oceanic heat flux forcing. Hence, to resolve the dynamics of the SIPL at large spatio-temporal scales, better understanding and formulation of water column processes is a key prerequisite. Oceanic processes were considered in more detail in other sea ice growth studies (Buffo et al., 2018; Dempsey et al., 2010) but remain generally elusive. The contribution of local and remote influences in terms of frazil crystal fluxes are not well understood (e.g., Cheng et al., 2019; Robinson et al., 2014), and the growth of crystals is not well connected with hydrodynamics and seawater characteristics (e.g., Rees Jones & Wells, 2018). Such aspects could be explored with dedicated field experiments or large-scale ocean-sea ice simulations. In this sense, our study opens perspectives, as we see the possibility to connect frazil ice in the ocean to the development of an SIPL.

The model simulates generally expected haline properties in both consolidated ice and within the SIPL. However, we still view the properties and water circulation in the SIPL (Robinson et al., 2014, 2017) as particularly uncertain. We used the salinity scheme of GN1315 and Rees Jones and Worster (2014), that assumes infinitely narrow brine channels and a return upwards flow in the rest of the ice. Such a scheme seems to capture some of the key features of liquid convection for the SIPL, as a Rayleigh number-driven convection probably embraces some of the reality of liquid convection in the SIPL. Progress could come from in-situ observations, which will be challenging, or high-resolution fluid dynamic simulations that would directly resolve the circulation of the liquid and its connection with the ocean. However, these may suffer from poor constraints on permeability. In this respect, the disregard of ocean shear flow is another source of uncertainty. Finally, we remind the reader that our knowledge of the SIPL is very poor during the decay period, and that large uncertainties exist at that time.

For biogeochemical applications, model details on brine circulation could prove important because brine circulation in the SIPL is presumably the key nutrient supply mechanism required to explain the tremendous biological productivity in the SIPL (Günther & Dieckmann, 1999). High dimethyl sulfide concentrations near the platelet ice transition were also highlighted by Carnat et al. (2014). Conversely, biogeochemical observations in the SIPL may provide indirect constraints on nutrient fluxes and on fluid circulation in the SIPL.

5. Summary and Conclusions

We now return to the questions posed in the Introduction. We have shown that a well-adjusted 1D mushy-layer sea ice model, thermally forced by atmospheric and oceanic conditions typical of the coastal McMurdo Sound area, Ross Sea, Antarctica, using standard, published values for model free parameters can reproduce a realistic, highly porous and isothermal SIPL consistent with observed sea ice mass, heat and salt balance observations. A key adjustment to the model was to set the initial brine fraction to ~75%, following earlier works (e.g., Hoppmann, Nicolaus, Hunkeler, et al., 2015; Wongpan et al., 2015). With such a value, the SIPL growth costs less energy, and is about three times more rapid than for typical congelation sea ice.

Our simulations shed light on the thermodynamic mechanisms driving the formation of the SIPL. The simulated SIPL develops once conductive heat fluxes are insufficient to cause internal freezing of the new, highly porous ice formed from sensible heat loss imposed by a supercooled ocean. Such conditions occur when consolidated ice and snow are thick enough to provide the required level of insulation. Once the temperature gradient in the consolidated ice reduces sufficiently for an SIPL to develop, the sea ice growth rate is no longer bounded by thickness and is solely dependent on thermal forcing from the ocean. Unbounded growth rates are consistent with the large SIPL thicknesses observed in several instances (in excess of 8 m, Hughes et al., 2014; Langhorne et al., 2015).

Our simulations also highlight thermo-haline processes resulting from large brine fractions, stabilizing the SIPL. The low thermal diffusivity inhibits both temperature and porosity changes in the SIPL and, in turn, hinders the development of a temperature gradient that would favor the SIPL decay. This mechanism constitutes a stabilizing feedback to the SIPL. Another stabilizing feedback is that brine convection strengthens the porosity contrast between the SIPL and the consolidated ice above. Three vertical layers are sufficient to qualitatively resolve the mechanisms driving SIPL development, whereas 10 layers result in increased accuracy of the solution. This suggests that low-cost representations of the SIPL in large-scale climate models can be achieved.

Substantial uncertainties remain regarding our understanding of the SIPL in a general oceanographic, climate and ecosystem context. The water column processes controlling the flux of crystals toward the sea ice base (Buffo et al., 2018) exert primary control on the large-scale distribution and seasonality of the SIPL (Cheng et al., 2019). However, how the ice crystal nucleation rate is distributed in space—vertically and horizontally—and in time, as a function of water properties and circulation, remains poorly known. Also, the high biological productivity of the SIPL (Arrigo, 2017; Günther & Dieckmann, 1999) relies upon nutrient supply pathways and processes that are essentially unexplained. In particular, natural and forced liquid convection in the SIPL remains practically undocumented from observations (Robinson et al., 2014, 2017).

The ability of the proposed 3-layer model to simulate an SIPL shows promise to address these issues on a large-scale and provides insight into the physical processes within the SIPL.

Data Availability Statement

The temperature data used in this study to derive oceanic heat flux at site G (2009B) following Gough, Mahoney, Langhorne, Williams, Robinson, et al. (2012) can be obtained from https://doi.pangaea.de/10.1594/PANGAEA.880163. Antarctic Mapping Tools for MATLAB (Greene et al., 2017) and cmocean colormap (Thyng et al., 2016) were used to produce figures. The LIM1D (Louvain-la-Neuve Sea Ice Model: LIM1D) is available at http://forge.ipsl.jussieu.fr/lim1d, revision #3.20.

References

Arrigo, K. R. (2017). Sea ice as a habitat for primary producers. In D. N. Thomas (Ed.), *Sea ice* (pp. 352–369). John Wiley & Sons, Ltd. https://doi.org/10.1002/9781118778371.ch14

Assur, A. (1960). *Composition of sea ice and its tensile strength: United States Army Cold Regions Research and Engineering Laboratory* (Tech. Rep.). Research Report 44.

Bitz, C. M., & Lipscomb, W. H. (1999). An energy-conserving thermodynamic model of sea ice. *Journal of Geophysical Research*, *104*(C7), 15669–15677. https://doi.org/10.1029/1999jc900100

Buffo, J. J., Schmidt, B. E., & Huber, C. (2018). Multiphase reactive trans- port and platelet ice accretion in the sea ice of McMurdo Sound, Antarctica. *Journal of Geophysical Research: Oceans*, *123*(1), 324–345. https://doi.org/10.1002/2017jc013345

Carnat, G., Zhou, J., Papakyriakou, T., Delille, B., Goossens, T., Haskell, T., et al. (2014). Physical and biological controls on DMS,P dynamics in ice shelf-influenced fast ice during a winter-spring and a spring-summer transitions. *Journal of Geophysical Research: Oceans*, *119*(5), 2882–2905. https://doi.org/10.1002/2013jc009381

Castelli, V., Stanley, E., & Fischer, E. (1974). The thermal conductivity of seawater as a function of pressure and temperature. *Deep-Sea Research and Oceanographic Abstracts*, *21*(4), 311–319. https://doi.org/10.1016/0011-7471(74)90102-8

Cheng, C., Jenkins, A., Holland, P. R., Wang, Z., Liu, C., & Xia, R. (2019). Responses of sub-ice platelet layer thickening rate and frazil-ice concentration to variations in ice-shelf water supercooling in McMurdo Sound, Antarctica. *The Cryosphere*, *13*(1), 265–280. https://doi.org/10.5194/tc-13-265-2019

Courant, R., Friedrichs, K., and Lewy, H. (1967). On the partial difference equations of mathematical physics. *IBM Journal of Research and Development*, *11*(2), 215–234. https://doi.org/10.1147/rd.112.0215

Dempsey, D. E., Langhorne, P. J., Robinson, N. J., Williams, M. J. M., Haskell, T. G., & Frew, R. D. (2010). Observation and modeling of platelet ice fabric in McMurdo Sound, Antarctica. *Journal of Geophysical Research*, *115*(C1). https://doi.org/10.1029/2008jc005264

Efimova, N. A. (1961). On methods of calculating monthly values of net longwave radiation. *Meteorologiya i Gidrologiya*, *10*, 28–33.

Freitag, J. (1999). The hydraulic properties of Arctic sea-ice–Implications for the small scale particle transport. *Reports on Polar Research*, *325*, 1–150.

Gough, A. J., Mahoney, A. R., Langhorne, P. J., Williams, M. J. M., & Haskell, T. G. (2012). Sea ice salinity and structure: A winter time series of salinity and its distribution. *Journal of Geophysical Research*, *117*(C3), C03008. https://doi.org/10.1029/2011jc007527

Gough, A. J., Mahoney, A. R., Langhorne, P. J., Williams, M. J. M., Robinson, N. J., & Haskell, T. G. (2012). Signatures of supercooling: McMurdo Sound platelet ice. *Journal of Glaciology*, *58*(207), 38–50. https://doi.org/10.3189/2012jog10j218

Gow, A. J., Ackley, S. F., Govoni, J. W., & Weeks, W. F. (1998, mar). Physical and structural properties of land-fast sea ice in McMurdo Sound, Antarctica. In *Antarctic sea ice: Physical processes, interactions and variability* (pp. 355–374). American Geophysical Union. https://doi.org/10.1029/ar074p0355

Greene, C. A., Gwyther, D. E., & Blankenship, D. D. (2017). Antarctic mapping tools for Matlab. *Computers & Geosciences*, *104*, 151–157. https://doi.org/10.1016/j.cageo.2016.08.003

Griewank, P. J., & Notz, D. (2013). Insights into brine dynamics and sea ice desalination from a 1-D model study of gravity drainage. *Journal of Geophysical Research: Oceans*, *118*(7), 3370–3386. https://doi.org/10.1002/jgrc.20247

Griewank, P. J., & Notz, D. (2015). A 1-D modeling study of Arctic sea-ice salinity. *The Cryosphere*, *9*(1), 305–329. https://doi.org/10.5194/tc-9-305-2015

Günther, S., & Dieckmann, G. S. (1999). Seasonal development of algal biomass in snow-covered fast ice and the underlying platelet layer in the Weddell Sea, Antarctica. *Antarctic Science*, *11*(03), 305–315. https://doi.org/10.1017/s0954102099000395

Holland, P. R., & Feltham, D. L. (2006). The effects of rotation and ice shelf topography on frazil-laden ice shelf water plumes. *Journal of Physical Oceanography*, *36*(12), 2312–2327. https://doi.org/10.1175/jpo2970.1

Hoppmann, M., Nicolaus, M., Hunkeler, P. A., Heil, P., Behrens, L.-K., König-Langlo, G., & Gerdes, R. (2015). Seasonal evolution of an ice-shelf influenced fast-ice regime, derived from an autonomous thermistor chain. *Journal of Geophysical Research: Oceans*, *120*(3), 1703–1724. https://doi.org/10.1002/2014jc010327

Hoppmann, M., Nicolaus, M., Paul, S., Hunkeler, P. A., Heinemann, G., Willmes, S., et al. (2015). Ice platelets below Weddell Sea landfast sea ice. *Annals of Glaciology*, *56*(69), 175–190. https://doi.org/10.3189/2015aog69a678

Hoppmann, M., Richter, M. E., Smith, I. J., Jendersie, S., Langhorne, P. J., Thomas, D. N., & Dieckmann, G. S. (2020). Platelet ice, the Southern Ocean's hidden ice: A review. *Annals of Glaciology*, *61*(83), 341–368. https://doi.org/10.1017/aog.2020.54

Hughes, K. G., Langhorne, P. J., Leonard, G. H., & Stevens, C. L. (2014). Extension of an Ice Shelf Water plume model beneath sea ice with application in McMurdo Sound, Antarctica. *Journal of Geophysical Research: Oceans*, *119*(12), 8662–8687. https://doi.org/10.1002/2013jc009411

Hunke, E. C., Notz, D., Turner, A. K., & Vancoppenolle, M. (2011). The multi-phase physics of sea ice: A review for model developers. *The Cryosphere*, *5*(4), 989–1009. https://doi.org/10.5194/tc-5-989-2011

Hunkeler, P. A., Hoppmann, M., Hendricks, S., Kalscheuer, T., & Gerdes, R. (2016). A glimpse beneath Antarctic sea ice: Platelet layer volume from multi-frequency electromagnetic induction sounding. *Geophysical Research Letters*, *43*(1), 222–231. https://doi.org/10.1002/2015gl065074

Jacobs, J. (1978). Energy budget studies in relation to fast-ice breakup processes in Davis Strait. In R.G. Barry and J.D. Jacobs (Eds.), *Radiation climate of Broughton Island* (pp. 105–120). INSTAAR, University of Colorado.

Jutras, M., Vancoppenolle, M., Lourenço, A., Vivier, F., Carnat, G., Madec, G., et al. (2016). Thermodynamics of slush and snow–ice formation in the Antarctic sea-ice zone. *Deep Sea Research Part II: Topical Studies in Oceanography*, *131*, 75–83. https://doi.org/10.1016/j.dsr2.2016.03.008

Langhorne, P. J., Hughes, K. G., Gough, A. J., Smith, I. J., Williams, M. J. M., Robinson, N. J., et al. (2015). Observed platelet ice distributions in Antarctic sea ice: An index for ocean-ice shelf heat flux. *Geophysical Research Letters*, *42*(13), 5442–5451. https://doi.org/10.1002/2015gl064508

Lecomte, O., Fichefet, T., Vancoppenolle, M., Domine, F., Massonnet, F., Mathiot, P., et al. (2013). On the formulation of snow thermal conductivity in large-scale sea ice models. *Journal of Advances in Modeling Earth Systems*, *5*(3), 542–557. https://doi.org/10.1002/jame.20039

Leonard, G. H., Purdie, C. R., Langhorne, P. J., Haskell, T. G., Williams, M. J. M., & Frew, R. D. (2006). Observations of platelet ice growth and oceanographic conditions during the winter of 2003 in McMurdo Sound, Antarctica. *Journal of Geophysical Research*, *111*(C4), C04012. https://doi.org/10.1029/2005jc002952

Maykut, G. A. (1986). The surface heat and mass balance. In *The geophysics of sea ice* (pp. 395–463). Springer. https://doi.org/10.1007/978-1-4899-5352-0_6

McPhee, M. G., Stevens, C. L., Smith, I. J., & Robinson, N. J. (2016). Turbulent heat transfer as a control of platelet ice growth in supercooled under-ice ocean boundary layers. *Ocean Science*, *12*(2), 507–515. https://doi.org/10.5194/os-12-507-2016

Moreau, S., Vancoppenolle, M., Delille, B., Tison, J.-L., Zhou, J., Kotovitch, M., et al. (2015). Drivers of inorganic carbon dynamics in first-year sea ice: A model study. *Journal of Geophysical Research: Oceans*, *120*(1), 471–495. https://doi.org/10.1002/2014jc010388

Notz, D., & Worster, M. G. (2008). In situ measurements of the evolution of young sea ice. *Journal of Geophysical Research*, *113*(C3), C03001. https://doi.org/10.1029/2007jc004333

Notz, D., & Worster, M. G. (2009). Desalination processes of sea ice revisited. *Journal of Geophysical Research*, *114*(C5), C05006. https://doi.org/10.1029/2008jc004885

Pringle, D. J., Eicken, H., Trodahl, H. J., & Backstrom, L. G. E. (2007). Thermal conductivity of landfast Antarctic and Arctic sea ice. *Journal of Geophysical Research*, *112*, C04017. https://doi.org/10.1029/2006JC003641

Rees Jones, D. W., & Wells, A. J. (2018). Frazil-ice growth rate and dynamics in mixed layers and sub-ice-shelf plumes. *The Cryosphere*, *12*(1), 25–38. https://doi.org/10.5194/tc-12-25-2018

Rees Jones, D. W., & Worster, M. G. (2014). A physically based parameterization of gravity drainage for sea-ice modeling. *Journal of Geophysical Research: Oceans*, *119*(9), 5599–5621. https://doi.org/10.1002/2013jc009296

Robinson, N. J., Stevens, C. L., & McPhee, M. G. (2017). Observations of amplified roughness from crystal accretion in the sub-ice ocean boundary layer. *Geophysical Research Letters*, *44*(4), 1814–1822. https://doi.org/10.1002/2016GL071491

Robinson, N. J., Williams, M. J. M., Stevens, C. L., Langhorne, P. J., & Haskell, T. G. (2014). Evolution of a supercooled Ice Shelf Water plume with an actively growing subice platelet matrix. *Journal of Geophysical Research: Oceans*, *119*(6), 3425–3446. https://doi.org/10.1002/2013jc009399

Sakatume, S., & Seki, N. (1978). On the thermal properties of ice and snow in a low temperature region. *Transactions of the Japan Society of Mechanical Engineers*, *44*(382), 2059–2069. https://doi.org/10.1299/kikai1938.44.2059

Schmidt, G. A., Bitz, C. M., Mikolajewicz, U., & Tremblay, L.-B. (2004). Ice–ocean boundary conditions for coupled models. *Ocean Modelling*, *7*(1–2), 59–74. https://doi.org/10.1016/s1463-5003(03)00030-1

Semtner, A. J. (1976). A model for the thermodynamic growth of sea ice in numerical investigations of climate. *Journal of Physical Oceanography*, *6*(3), 379–389. https://doi.org/10.1175/1520-0485(1976)006<0379:Amfttg>2.0.Co;2

Shine, K. P., & Henderson-Sellers, A. (1985). The sensitivity of a thermodynamic sea ice model to changes in surface albedo parameterization. *Journal of Geophysical Research*, *90*(D1), 2243. https://doi.org/10.1029/jd090id01p02243

Smedsrud, L. H., & Skogseth, R. (2006). Field measurements of Arctic grease ice properties and processes. *Cold Regions Science and Technology*, *44*, 171–183. https://doi.org/10.1016/j.coldregions.2005.11.002

Smith, I. J., Gough, A. J., Langhorne, P. J., Mahoney, A. R., Leonard, G. H., Hale, R. V., et al. (2015). First-year land-fast Antarctic sea ice as an archive of ice shelf meltwater fluxes. *Cold Regions Science and Technology*, *113*, 63–70. https://doi.org/10.1016/j.coldregions.2015.01.007

Smith, I. J., Langhorne, P. J., Frew, R. D., Vennell, R., & Haskell, T. G. (2012). Sea ice growth rates near ice shelves. *Cold Regions Science and Technology*, *83–84*, 57–70. https://doi.org/10.1016/j.coldregions.2012.06.005

Steiner, N., Deal, C., Lannuzel, D., Lavoie, D., Massonnet, F., Miller, L. A., et al. (2016). What sea-ice biogeochemical modellers need from observers. *Elementa: Science of the Anthropocene*, *4*, 000084. https://doi.org/10.12952/journal.elementa.000084

Thomas, M., Vancoppenolle, M., France, J. L., Sturges, W. T., Bakker, D. C. E., Kaiser, J., & Glasow, R. (2020). Tracer measurements in growing sea ice support convective gravity drainage parameterizations. *Journal of Geophysical Research: Oceans*, *125*(2), e2019JC015791. https://doi.org/10.1029/2019jc015791

Thyng, K., Greene, C., Hetland, R., Zimmerle, H., & DiMarco, S. (2016). True colors of oceanography: Guidelines for effective and accurate colormap selection. *Oceanography*, *29*(3), 9–13. https://doi.org/10.5670/oceanog.2016.66

Turner, A. K., & Hunke, E. C. (2015). Impacts of a mushy-layer thermodynamic approach in global sea-ice simulations using the CICE sea-ice model. *Journal of Geophysical Research: Oceans*, *120*, 1253–1275. https://doi.org/10.1002/2014JC010358

Turner, A. K., Hunke, E. C., & Bitz, C. M. (2013). Two modes of sea-ice gravity drainage: A parameterization for large-scale modeling. *Journal of Geophysical Research: Oceans*, *118*, 2279–2294. https://doi.org/10.1002/jgrc.20171

Vancoppenolle, M., Goosse, H., de Montety, A., Fichefet, T., Tremblay, B., & Tison, J.-L. (2010). Modeling brine and nutrient dynamics in Antarctic sea ice: The case of dissolved silica. *Journal of Geophysical Research*, *115*(C2), C02005. https://doi.org/10.1029/2009jc005369

Vancoppenolle, M., Madec, G., Thomas, M., & McDougall, T. J. (2019). Thermodynamics of sea ice phase composition revisited. *Journal of Geophysical Research: Oceans*, *124*(1), 615–634. https://doi.org/10.1029/2018jc014611

Vancoppenolle, M., Timmermann, R., Ackley, S. F., Fichefet, T., Goosse, H., Heil, P., et al. (2011). Assessment of radiation forcing data sets for large-scale sea ice models in the Southern Ocean. *Deep Sea Research Part II: Topical Studies in Oceanography*, *58*(9–10), 1237–1249. https://doi.org/10.1016/j.dsr2.2010.10.039

Wells, A. J., Wettlaufer, J. S., & Orszag, S. A. (2011). Brine fluxes from growing sea ice. *Geophysical Research Letters*, *38*(4), L04501. https://doi.org/10.1029/2010GL046288

Wongpan, P., Hughes, K. G., Langhorne, P. J., & Smith, I. J. (2018). Brine convection, temperature fluctuations, and permeability in winter Antarctic land-fast sea ice. *Journal of Geophysical Research: Oceans*, *123*(1), 216–230. https://doi.org/10.1002/2017jc012999

Wongpan, P., Langhorne, P. J., Dempsey, D. E., Hahn-Woernle, L., & Sun, Z. (2015). Simulation of the crystal growth of platelet sea ice with diffusive heat and mass transfer. *Annals of Glaciology*, *56*(69), 127–136. https://doi.org/10.3189/2015aog69a777

Worster, M. G. (1992). Instabilities of the liquid and mushy regions during solidification of alloys. *Journal of Fluid Mechanics*, *237*, 649–669. https://doi.org/10.1017/s0022112092003562